Single-site and multisite resonant photoemission theory studied by Keldysh Green's functions

Hiroko Arai* and Takashi Fujikawa
Graduate School for Science, Chiba University, Yayoi-cho 1-33, Inage, Chiba 263-8522, Japan
(Received 13 October 2004; revised manuscript received 24 May 2005; published 1 August 2005)

Single (on-site) and multisite (multiatom) resonant photoemission (MARPE) processes are systematically studied by use of nonrelativistic Keldysh Green's function theory. We apply skeleton expansion in terms of renormalized one-electron Green's functions. In this theoretical framework we discuss the importance of the radiation field screening and the dynamically polarized part W_p in the screened Coulomb propagator. The radiation field screening plays a crucial role in observing the MARPE: We obtain expressions of the resonant processes (on site and multiatom) in terms of an x-ray absorption factor whose imaginary part is proportional to the x-ray absorption intensity. If we neglect W_p, the calculated MARPE intensity is much smaller than the observed one. We also point out the importance of the structure factor in the MARPE analyses. Typically highly symmetric atomic arrangement around a photoemitting atom provides us with no MARPE signal, but outermost oxygen atoms give rise to considerably strong MARPE because of symmetry lowering. On the other hand, low symmetric systems like rutile, perovskite, and α-alumina (Fe_2O_3) structures can give rise to finite MARPE even in the case of photoemission from inner layers of perfect crystals. The polarization dependence of the MARPE follows the same selection rule as the main photoemission processes, whereas the O 1*s* MARPE from Fe_2O_3 shows a rather complicated rule. These specific features of MARPE provide useful local structural information.

DOI: 10.1103/PhysRevB.72.075102 PACS number(s): 79.60.−i, 68.35.−p, 78.20.Ci, 78.70.Dm

I. INTRODUCTION

A useful and practical many-body approach to x-ray photoemission spectroscopy (XPS) analyses has been developed by Bardyszewski and Hedin by use of projection operator techniques.[1] Further refinement is found in Ref. 2. The above theoretical approach is practically useful to describe the photoemission processes in terms of damping photoelectron wave functions under the influence of the optical potentials. This direct approach, however, has not been applied to study resonant photoemission processes.

As an alternative approach, first-principle XPS theories based on Keldysh Green's functions have been developed.[3–8] These theories gave formally exact perturbation expansion of the photoemission intensity. The present authors have used skeleton expansion in terms of renormalized one-electron Green's functions.[7] Further refinement to include radiation field screening is also proposed.[8] In this approach we can analyze XPS spectra excited from systems at finite temperature and from nonequilibrium systems.

Recent experimental developments of multiatom resonant photoemission (MARPE) permit direct determination of near-neighbor atomic identities[9,10] because MARPE occurs when the photon energy is tuned to be a core-level absorption edge of an atom neighboring the emitting atom. Extended x-ray absorption fine structure (EXAFS) analyses of the backscattering amplitude can also identify the backscattering atomic species. It is, however, quite difficult to distinguish near-neighbor atoms such as Mn from Fe or Co from the EXAFS analyses, because their backscattering amplitudes $f(\pi)$'s are quite similar. MARPE can distinguish them since their absorption edge energies are quite different. So far much effort has been paid to observe MARPE for some transition metal oxide, magnetic thin films, molecular adsorption system, and so on.[10–18] Some authors insist that they were not able to observe the MARPE, whereas some authors were able to observe the resonant features. Several simple but crude theoretical approaches are also available.[10,11,19] In Ref. 11, a microscopic quantum mechanics approach including retardation effect is presented to explain the MARPE effect and also the macroscopic x-ray optics approach in Ref. 10. An x-ray optics approach can successfully describe MARPE effects using experimental optical constants such as x-ray absorption coefficient; however, it is built on the classical theory. It is thus hard to give credit to this macroscopic theory for the description of the microscopic processes. An *ab initio* molecular orbital method is also proposed by Carravetta and Ågren;[19] however, they consider a two-step picture of the MARPE effect, in which no interference term is included, and only small molecules are calculated. These works have paid no attention to the controversial discussion due to the structure factor sensitive to local arrangement of nearest-neighbor atoms around a photoelectron emitter.[7]

In this paper, by use of the Keldysh Green's functions, we study the radiation field screening and the polarization part W_p of screened Coulomb interaction $W(W=v+W_p)$ in the MARPE analyses, which were also considered in brief in our preliminary paper.[20] We demonstrate the importance of W_p to obtain intense MARPE comparable with the observed one. We obtain new approximate formulas of the resonant on-site and multisite resonant photoemission processes in terms of x-ray absorption factors $f_d(\omega)$ of the deep cores where $-2\,\mathrm{Im}\,f_d(\omega)$ is just proportional to the x-ray absorption intensity. Further extensive discussion is also given to the structure factors which play a dominant role in observing the MARPE. For highly symmetric atomic arrangements such as O_h and T_d, no MARPE is expected to be observed because

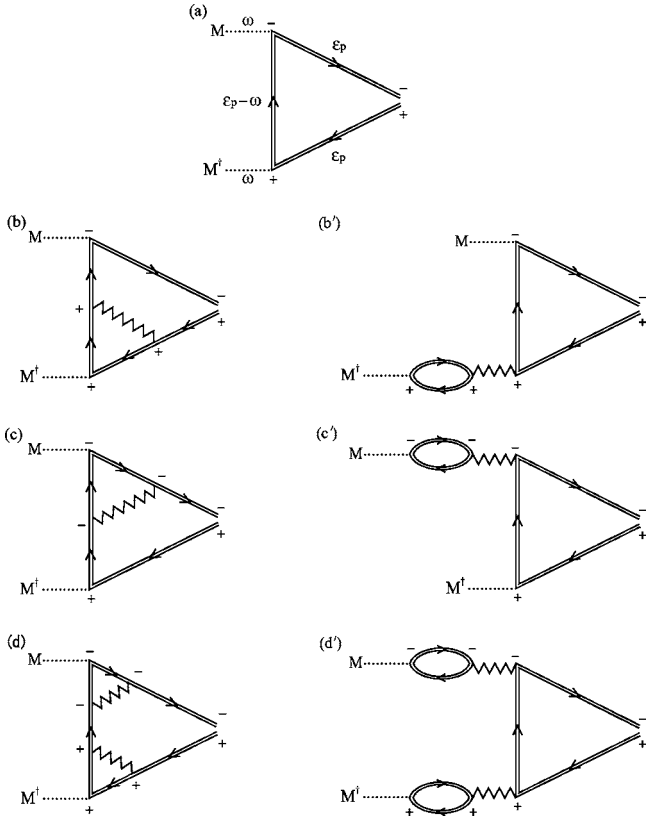

FIG. 1. Keldysh diagrams that contribute to resonant processes. Diagrams (b′)–(d′) partly include the radiation field screening.

the structure factors should vanish for these symmetries. On the other hand, low symmetric systems, such as rutile, perovskite, and Fe_2O_3 structures, can provide a finite MARPE signal even for the photoemission from inner layers in the perfect crystals.

II. MARPE THEORY

In this section we derive some useful formulas to describe the resonant photoemission processes, including the MARPE, based on the Keldysh Green's function theory.[7,8]

A. Resonant XPS theory

Figure 1 shows the Keldysh diagrams contributing to the resonant photoemission processes. When the end points of the screened Coulomb W are on the same time legs, the diagrams contribute to virtual excitation. When they are on different time legs, the diagrams contribute to extrinsic loss. The interaction W can be written as the sum by noting that $W=v+v\pi v$ (π is reducible polarization propagator),

$$W(x,x';\omega) = v(\mathbf{r}-\mathbf{r}') + W_p(x,x';\omega), \quad x=(\mathbf{r},\sigma), \quad (1)$$

where v is the bare Coulomb interaction, and $W_p=v\pi v$ is the dynamically polarized potential. The diagram in Fig. 1(a) describes typical photoemission processes.[1,6] Of course, this term cannot describe resonant and extrinsic loss photoemission processes. The diagrams in Figs. 1(b)–1(d) cannot explain the MARPE spectra, but they contribute to the on-site resonant photoemission.

So far, the radiation field screening vertex contribution as shown by Figs. 1(b′)–1(d′) has been supposed to be quite small,[5] and has been neglected. Near the resonance energy, however, the radiation field screening is crucial to interpret the resonance effects in XPS and x-ray absorption fine structure (XAFS).[8] We add all terms responsible for the resonant photoemission processes including the radiation field screening vertex, then we obtain

$$\mathbf{j}_{\mathbf{p}}^{(a)} + \mathbf{j}_{\mathbf{p}}^{(b)} + \cdots + \mathbf{j}_{\mathbf{p}}^{(d')} = \frac{\mathbf{p}}{2\pi\Gamma}\sum_n \left|\langle f_{\mathbf{p}}^-|\Delta|g_n\rangle + i\langle f_{\mathbf{p}}^-|X(\omega)|g_n\rangle + i\langle f_{\mathbf{p}}^-|Z(\omega)|g_n\rangle\right|^2 \delta[\varepsilon_p + E_n(N-1) - \omega - E_0(N)]. \quad (2)$$

The hole Dyson orbitals g_n, the bound particle Dyson orbital f_q, and the resonant operators [$X(\omega)$ from Figs. 1(b)–1(d) and $Z(\omega)$ from Figs. 1(b′)–1(d′)] are defined in our previous paper.[7] The scattering particle Dyson orbital $f_{\mathbf{p}}^-(x)$ approaches to the plane wave outside the solids far from the target; however, in solids its amplitude damps under the influence of the optical potential Σ.[21–26] Explicit derivation of the optical potential for $f_{\mathbf{p}}^-$ is given in Appendix A.

In the simple approximation $W\approx v$, the amplitude $\langle f_{\mathbf{p}}^-|X|g_n\rangle$ is given by[7]

$$i\langle f_{\mathbf{p}}^-|X|g_n\rangle \approx -\sum_{sj}\frac{\langle f_s|\Delta|g_j\rangle\langle f_{\mathbf{p}}^- g_j|f_s g_n\rangle}{\omega+\varepsilon_j-\varepsilon_s+i\eta}. \quad (3)$$

The two-electron integral $\langle f_1 f_2|f_3 f_4\rangle$ is defined as usual in Eq. (4.13) in our previous paper (Ref. 7). In MARPE processes, both g_j and g_n are localized on different atoms, so that the differential overlap between them has to be negligibly small. Even though we include the polarization part of W, we can neglect $\langle f_{\mathbf{p}}^-|X|g_n\rangle$ for the discussion of MARPE for the same reason.

The nonlocal energy-dependent operator $Z(\omega)$, due to the radiation field screening, is given by use of the screened Coulomb interaction W,

$$i\langle f_{\mathbf{p}}^-|Z(\omega)|g_n\rangle = \sum_{sj}\left[\frac{\langle f_{\mathbf{p}}^- g_j|W(\omega)|g_n f_s\rangle}{\omega+\varepsilon_j-\varepsilon_s+i\eta}\langle f_s|\Delta|g_j\rangle - \frac{\langle f_{\mathbf{p}}^- f_s|W(\omega)|g_n g_j\rangle}{\omega-\varepsilon_j+\varepsilon_s-i\eta}\langle g_j|\Delta|f_s\rangle\right]. \quad (4)$$

The second term is negligibly small in comparison with the first term because of the large energy denominator as discussed before. In the lowest order, $W\approx v$ approximation together with (3), we thus obtain a useful approximate formula for the MARPE and on-site resonant photoemission analyses,

$$I(\mathbf{p},\omega) \propto \sum_n \left|\langle f_{\mathbf{p}}^-|\Delta|g_n\rangle + \sum_{sj}\frac{\langle f_{\mathbf{p}}^- g_j||g_n f_s\rangle\langle f_s|\Delta|g_j\rangle}{\omega+\varepsilon_j-\varepsilon_s+i\Gamma_r}\right|^2 \times\delta[\varepsilon_p + E_n(N-1) - \omega - E_0(N)], \quad (5)$$

where $\langle f_1 f_2||f_3 f_4\rangle = \langle f_1 f_2|f_3 f_4\rangle - \langle f_1 f_2|f_4 f_3\rangle$. We should note

that the photoelectron current $\mathbf{j_p}$ is closely related to the photoemission intensity $I(\mathbf{p},\omega)$,[3]

$$\mathbf{j_p} \approx \frac{\mathbf{p}}{\Gamma} I(\mathbf{p},\omega). \tag{6}$$

The first term on the right-hand side of Eq. (5) is the ordinary direct photoemission amplitude from the Dyson orbital g_n to $f_{\mathbf{p}}^-$, where the second term has the resonant contribution because it parametrically depends on ω in the denominator. This formula shows resonant behavior at $\omega \approx \varepsilon_s - \varepsilon_j$ as observed in Ref. 7; however, as demonstrated below, this approximation is not sufficient to precisely explain the MARPE; the predicted MARPE intensity is still much smaller than the observed MARPE. We should note that Eq. (5) is also applicable to the analyses of on-site resonant photoemission spectra.

We next study the effect of the polarization part of W, that is, $W_p = v\pi v$.[20] We note that the reducible polarization propagator π is related to the irreducible polarization P, $\pi = P + PWP$. Here we use an approximation $\pi \approx P_0$, where P_0 is the lowest order skeleton expansion of P. The polarization part in the element $i\langle f_{\mathbf{p}}^- | Z(\omega) | g_n \rangle$ is given by neglecting the terms with large energy denominator,[20]

$$\begin{aligned}\langle f_{\mathbf{p}}^- g_j | W_p(\omega) | g_n f_s \rangle &\approx \langle f_{\mathbf{p}}^- g_j | v P_0 v | g_n f_s \rangle \\ &\approx \sum_{mq} \frac{\langle f_{\mathbf{p}}^- g_m | g_n f_q \rangle \langle g_j f_q | f_s g_m \rangle}{\omega + \varepsilon_m - \varepsilon_q + i\eta}.\end{aligned} \tag{7}$$

To specify the problem, let us consider O 1s MARPE in MnO, where ω is close to the Mn 2p threshold. In this case g_m and g_j are approximated by Mn 2p core functions ϕ_d multiplied by intrinsic amplitudes, and g_n is approximated by the O 1s function ϕ_c, f_s and f_q by Mn 3d or εd, and ε_m corresponds to the threshold of the Mn 2p core excitation $\varepsilon_m \sim -I_d = \varepsilon_d$. We stress the importance of the skeleton expansion; in the denominator of Eq. (7) we have exact ionization energy $-\varepsilon_m$ instead of orbital energy in the Hartree-Fock approximation. Since the incident x-ray energy ω is close to the Mn 2p threshold ($\omega \sim -\varepsilon_m$), Eq. (7) has a large contribution near the core excitation energy.

Let us rewrite the second term in the absolute value in Eq. (5). We neglect the exchange term, that is, $\langle f_{\mathbf{p}}^- g_j || g_n f_s \rangle \sim \langle f_{\mathbf{p}}^- g_j | g_n f_s \rangle$. As discussed, this approximation causes no serious problem for the MARPE analyses, whereas it may introduce a small amount of error for the on-site resonant photoemission analyses. At first we consider the on-site resonance effects; the two core orbitals contributing to the resonance are localized on the same atom A. We thus have

$$\begin{aligned}&\sum_{mq} \frac{\langle f_{\mathbf{p}}^- g_m | g_n f_q \rangle \langle f_q | \Delta | g_m \rangle}{\omega + \varepsilon_m - \varepsilon_q + i\eta} \\ &\quad \approx \sum_d \int dx_1 dx_2 dx_3 f_{\mathbf{p}}^{-*}(x_1) \phi_d^*(x_2) \\ &\quad \times v(\mathbf{r}_1 - \mathbf{r}_2) \phi_c(x_1) \Delta(x_3) \phi_d(x_3) g_{sc}(x_2, x_3; \omega + \varepsilon_d),\end{aligned} \tag{8}$$

where the sum over d means that over m_d and the hole Dyson orbital $g_n(x)$ is approximated by $S_n^c \phi_c(x)$, whereas $g_m(x)$ is approximated by $S_m^d \phi_d(x)$; S_m^d and S_n^c are the intrinsic amplitudes associated with the core excitation from ϕ_d and ϕ_c. Both ϕ_c and ϕ_d are on the same atom. We only use one channel, $S_n^c \sim \delta_{n0}$, $S_m^d \sim \delta_{m0}$, for simplicity. The scattering Green's function g_{sc} in Eq. (8) is defined by

$$g_{sc}(x_2, x_3; \omega + \varepsilon_d) \equiv \sum_q \frac{f_q(x_2) f_q^*(x_3)}{\omega + \varepsilon_d - \varepsilon_q + i\eta}. \tag{9}$$

This function is the "particle" part of the retarded Green's function g^r.[28] We thus reduce the problem to the calculation of the Green's function g_{sc}. In the lowest approximation we only consider the contribution from the x-ray absorber A, and neglect scatterings from the neighboring atoms (one-site approximation of g_{sc}), which yields for the nonmagnetic systems

$$g_{sc}(\mathbf{r}_2, \mathbf{r}_3; \omega + \varepsilon_d) = \sum_L g_l(r_2, r_3; \omega + \varepsilon_d) Y_L^*(\hat{\mathbf{r}}_2) Y_L(\hat{\mathbf{r}}_3). \tag{10}$$

Substituting Eq. (10) into Eq. (8) we obtain

$$\text{Eq. (8)} = \langle f_{\mathbf{p}}^- | \lambda(\omega + \varepsilon_d, r) Y_{10}(\hat{\mathbf{r}}) | \phi_c \rangle, \tag{11}$$

$$\begin{aligned}\lambda(\omega + \varepsilon_d; r_1) \equiv \frac{2l_d + 1}{9} \sum_l (2l+1) \langle l_d 0 l 0 | 1 \rangle^2 \\ \times \int dr_2 dr_3 r_2^2 r_3^3 R_{l_d}(r_2) R_{l_d}(r_3) \frac{r_<}{r_>^2} \\ \times g_l(r_2, r_3; \omega + \varepsilon_d),\end{aligned} \tag{12}$$

where $r_< = \min(r_1, r_2)$, $r_> = \max(r_1, r_2)$, and R_{l_d} is the radial part of ϕ_d. As r_2 extends up to the size of the deep core ϕ_d, r_1 extends to that of the shallow core ϕ_c. We thus expect that $r_2 < r_1$ in Eq. (12), and we have another expression of λ,

$$\lambda(\omega + \varepsilon_d; r_1) = \frac{2l_d + 1}{9 r_1^2} \sum_l (2l+1) \langle l_d 0 l 0 | 1 \rangle^2 \hat{\rho}^A(\omega + \varepsilon_d)_l, \tag{13}$$

where $\hat{\rho}^A$ is defined later [see Eq. (28)]. On the other hand, the x-ray absorption factor from the deep core ϕ_d is given by

$$\begin{aligned}f_d(\omega) = -2 \sum_d \langle \phi_d | \Delta^* g_{sc}(\omega + \varepsilon_d) \Delta | \phi_d \rangle \approx -\frac{2l_d + 1}{6\pi} \sum_l (2l+1) \\ \times \langle l_d 0 l 0 | 1 \rangle^2 \hat{\rho}^A(\omega + \varepsilon_d)_l.\end{aligned} \tag{14}$$

The imaginary part of $f_d(\omega)$ is closely related to the corresponding x-ray absorption intensity. We thus have an interesting relation between $\lambda(\omega + \varepsilon_d, r)$ and $f_d(\omega)$,[20]

$$\lambda(\omega + \varepsilon_d, r) \approx -\frac{1}{r^2} \frac{2\pi f_d(\omega)}{3}. \tag{15}$$

As is well known from anomalous x-ray scattering, the amplitude $f_d(\omega)$ shows resonant behavior near the deep core threshold.[29,30] The scattering effects in g_{sc} (beyond the one-site approximation) give additional factors to the right-hand side of Eq. (10).

Next we consider the effects from W_p.[20] By using the approximations $W_p \sim v P_0 v$ and the single-site approximation for g_{sc} [see Eq. (10)], we have

$$\sum_{mq} \frac{\langle f_{\mathbf{p}}^- g_m | W_p(\omega) | g_n f_q \rangle \langle f_q | \Delta | g_m \rangle}{\omega + \varepsilon_m - \varepsilon_q + i\eta} \approx \langle f_{\mathbf{p}}^- | \lambda'(\omega + \varepsilon_d, r) Y_{10}(\hat{\mathbf{r}}) | \phi_c \rangle \tag{16}$$

where λ' is the radial integral including λ, g_l and R_{l_d},

$$\lambda'(\omega + \varepsilon_d, r_1) \equiv \frac{2l_d + 1}{9} \sum_l (2l+1) \langle l_d 0 l 0 | 1 \rangle^2 \times \int dr_2 dr_3 r_2^2 r_3^2 R_{l_d}(r_2) R_{l_d}(r_3) \frac{r_<}{r_>^2} \times g_l(r_2, r_3; \omega + \varepsilon_d) \lambda(\omega + \varepsilon_d, r_3), \tag{17}$$

where $r_> = \max(r_1, r_2)$, $r_< = \min(r_1, r_2)$. In the above integral, r_2 and r_3 should extend up to the size of the deep core ϕ_d, thus the approximation (15) is not safely used, but we can assume that $r_1 > r_2$, since r_1 extends up to the size of shallow core ϕ_c. We thus have an approximate formula of λ',

$$\lambda'(\omega + \varepsilon_d, r_1) \approx \frac{1}{r_1^2} \frac{2l_d + 1}{9} \sum_l (2l+1) \langle l_d 0 l 0 | 1 \rangle^2 \rho'^A(\omega + \varepsilon_d)_l, \tag{18}$$

where ρ'^A is defined later by Eq. (29). A further simplified but crude expression is obtained, if the approximation (15) is used in Eq. (18), and is also related to $f_d(\omega)$ but includes an additional factor $\tilde{f}_d(\omega)$ in the one-site approximation

$$\lambda'(\omega + \varepsilon_d, r) \approx \frac{1}{r^2} \left(\frac{2\pi}{3} \right)^2 f_d(\omega) \tilde{f}_d(\omega), \tag{19}$$

$$\tilde{f}_d(\omega) = -2 \sum_d \langle \phi_d | \Delta^* g_{sc}(\omega + \varepsilon_d) \tilde{\Delta} | \phi_d \rangle, \tag{20}$$

where $\tilde{\Delta} = Y_{10}(\hat{\mathbf{r}})/r^2$ is different from Δ in its radial dependence. Both f_d and $\tilde{f}_d$ follow the same selection rule in regard to orbital angular momentum.

From the above discussion, the on-site resonant XPS current intensity $I(\mathbf{p}, \omega)$ is represented in terms of the energy-dependent effective excitation operator Δ'

$$I(\mathbf{p}, \omega) \propto \left| \langle f_{\mathbf{p}}^- | \Delta'(\varepsilon_d + \omega, \mathbf{r}) | \phi_c \rangle \right|^2 \times \delta[\varepsilon_p + E_n(N-1) - \omega - E_0(N)], \tag{21}$$

where Δ' is defined by use of λ and λ' introduced [see Eqs. (15) and (18)],

$$\Delta'(\varepsilon_d + \omega, \mathbf{r}) = [r + \lambda(\varepsilon_d + \omega, r) + \lambda'(\varepsilon_d + \omega, r)] Y_{10}(\hat{\mathbf{r}}). \tag{22}$$

This excitation operator includes only $Y_{10}(\hat{\mathbf{r}})$ as the angular part, so that the selection rule is the same as that in the typical photoemission processes. The energy dependence, however, is quite different, because the resonant operators λ and λ' related to x-ray absorption factor f_d inevitably show the on-site resonant behaviors. X-ray absorption and/or x-ray anomalous scattering can be observed for all atoms; however, multisite resonant photoemission is not always observed. In the next section local structure around an emitter plays an important role to explain multisite resonant effects. We should note that the effective excitation operator Δ' has no contribution from the operator X in Eq. (2), which is much smaller than that from Z for nonmagnetic systems.

B. MARPE theory

The second term in Eq. (2) cannot describe MARPE even though we add the polarization part W_p because of a negligibly small differential overlap between deep and shallow core functions on different sites. We derived a useful MARPE formula in our previous work,[8] which is written in terms of spectral representation. In this section we present alternative MARPE formulas in terms of x-ray absorption factor f_d, which can be used to discuss x-ray anomalous scatterings and structure factors.

In the case where ϕ_c is on the site A and ϕ_d on the different site α as in the MARPE, the resonant terms [the first term in Eq. (4)] is rewritten by use of the approximation (10)

$$\sum_{sj} \frac{\langle f_s | \Delta | g_j \rangle \langle f_{\mathbf{p}}^- g_j | \phi_c f_s \rangle}{\omega + \varepsilon_j - \varepsilon_s + i\eta} = \sum_\alpha \sum_{m'} A(\mathbf{R}_\alpha, \omega)_{m'}^d \langle f_{\mathbf{p}}^- | r Y_{1m'}(\hat{\mathbf{r}}) | \phi_c \rangle, \tag{23}$$

$$\sum_{sj} \frac{\langle f_s | \Delta | g_j \rangle \langle f_{\mathbf{p}}^- g_j | W_p(\omega) | \phi_c f_s \rangle}{\omega + \varepsilon_j - \varepsilon_s + i\eta} = \sum_\alpha \sum_{m'} A'(\mathbf{R}_\alpha, \omega)_{m'}^d \langle f_{\mathbf{p}}^- | r Y_{1m'}(\hat{\mathbf{r}}) | \phi_c \rangle, \tag{24}$$

where the structure factor $A(\mathbf{R}_\alpha, \omega)_{m'}^d$ and the related factor $A'(\mathbf{R}_\alpha, \omega)_{m'}^d$ are slightly different from the previous one,[7]

$$A(\mathbf{R}_\alpha, \omega)_{m'}^d = \frac{4\pi}{3} \sum_{Lm_d} G(L_d 1 0 | L)^2 \hat{\rho}^\alpha(\omega + \varepsilon_d)_l y_{10,1m'}(\mathbf{R}_\alpha) = \frac{1}{3} \{ (l_d + 1) \hat{\rho}^\alpha(\omega + \varepsilon_d)_{l_d+1} + l_d \hat{\rho}^\alpha(\omega + \varepsilon_d)_{l_d-1} \} y_{10,1m'}(\mathbf{R}_\alpha), \tag{25}$$

$$A'(\mathbf{R}_\alpha, \omega)_{m'}^d = \frac{4\pi}{3} \sum_{Lm_d} G(L_d 1 0 | L)^2 \rho'^\alpha(\omega + \varepsilon_d)_l y_{10,1m'}(\mathbf{R}_\alpha) = \frac{1}{3} \{ (l_d + 1) \rho'^\alpha(\omega + \varepsilon_d)_{l_d+1} + l_d \rho'^\alpha(\omega + \varepsilon_d)_{l_d-1} \} y_{10,1m'}(\mathbf{R}_\alpha), \tag{26}$$

where $G(L_1 L_2 | L_3)$ is the Gaunt integral defined by $\int Y_{L_1} Y_{L_2} Y_{L_3}^* d\hat{\mathbf{r}}$ and

$$y_{LL'}(\mathbf{R}) = \frac{4\pi(-1)^l(2l+2l'-1)!!}{R^{l+l'+1}(2l-1)!!\,(2l'+1)!!} \times G(l+l',m-m',L'|L)Y_{l+l',m-m'}(\hat{\mathbf{R}}). \quad (27)$$

The integral $\hat{\rho}^{\alpha}$ and the related integral ρ'^{α} for the excitation from ϕ_d on the site α are defined by use of g_l^{α} [see Eq. (10)] and R_{l_d} (the radial part of ϕ_d),

$$\hat{\rho}^{\alpha}(\omega+\varepsilon_d)_l = \int R_{l_d}(r_2)R_{l_d}(r_3)g_l^{\alpha}(r_2,r_3;\omega+\varepsilon_d)r_2^3r_3^3dr_2dr_3, \quad (28)$$

$$\rho'^{\alpha}(\omega+\varepsilon_d)_l = \int R_{l_d}(r_2)R_{l_d}(r_3)g_l^{\alpha}(r_2,r_3;\omega+\varepsilon_d) \times \lambda(\omega+\varepsilon_d,r_3)r_2^3r_3^2dr_2dr_3. \quad (29)$$

Derivation of Eqs. (23)–(29) is briefly given in Appendix B. The structure factor $A(\mathbf{R}_{\alpha},\omega)_m^d$ is easily related to the x-ray absorption factor $f_d(\omega)$ at site α defined by Eq. (14) within the single-site approximation

$$A(\mathbf{R}_{\alpha},\omega)_{m'}^d = -\frac{2\pi}{3}f_d(\omega)y_{10,1m'}(\mathbf{R}_{\alpha}). \quad (30)$$

On the other hand, A' defined by Eq. (26) cannot be related to $f_d(\omega)$ but to a slightly different factor,

$$f_d''(\omega) = -2\sum_{m_d}\langle\phi_d|\Delta^* g_{sc}(\omega+\varepsilon_d)\lambda(\omega+\varepsilon_d)Y_{10}|\phi_d\rangle, \quad (31)$$

where $\lambda(\omega+\varepsilon_d,r)$ depends on photon energy and shows the resonant behavior. We thus have

$$A'(\mathbf{R}_{\alpha},\omega)_{m'}^d = -\frac{2\pi}{3}f_d''(\omega)y_{10,1m'}(\mathbf{R}_{\alpha}). \quad (32)$$

We should note that the factor $y_{10,1m}(\mathbf{R})$ decays as R^{-3}, so that only the nearest neighbors can dominantly contribute to MARPE. In comparison with the effective operator Δ' in the on-site resonant photoemission, the present effective operator Δ'' defined by Eq. (34) depends on the site α through $A(\mathbf{R}_{\alpha},\omega)_m^d$ and $A'(\mathbf{R}_{\alpha},\omega)_m^d$. The radial part $\lambda(\omega+\varepsilon_d,r)$ is reduced to Eq. (15) when r is larger than the size of core function ϕ_d, but in Eq. (29) r_3 is also in the region of the deep core function ϕ_d. Finally we obtain an explicit nonrelativistic MARPE formula similar to the on-site resonant photoemission intensity shown by Eq. (21),

$$I(\mathbf{p},\omega) \propto |\langle f_{\mathbf{p}}^-|\Delta''(\omega+\varepsilon_d,\mathbf{r})|\phi_c\rangle|^2 \times \delta[\varepsilon_p + E_n(N-1) - \omega - E_0(N)], \quad (33)$$

where

$$\Delta''(\omega+\varepsilon_d,\mathbf{r}) = \Delta(\mathbf{r}) + \sum_{m'}\left[\sum_{\alpha}(A(\mathbf{R}_{\alpha},\omega)_{m'}^d + A'(\mathbf{R}_{\alpha},\omega)_{m'}^d)\right]rY_{1m'}(\hat{\mathbf{r}}). \quad (34)$$

The effective electron-photon interaction operator Δ'' has an energy-dependent structure factor A and A' proportional to f_d and f_d'' so that multisite resonant effects are sensitive to the local structure around the emitter and show resonant behavior around the deep core threshold. The energy-dependent excitation operator Δ'' has the angular dependence $Y_{1\pm1}(\hat{\mathbf{r}})$ in addition to $Y_{10}(\hat{\mathbf{r}})$. As shown in the next section, however, the former can be neglected except for low symmetric systems like Fe_2O_3.

III. MARPE CALCULATIONS

So far we have pointed out the importance of the local structure[7] and radiation field screening[8] in MARPE analyses. Even though we include the latter effect, the calculated MARPE is much smaller than the observed one for MnO systems.[8] To overcome the difficulty we study the influence of W_p on MARPE. In this work, we calculate O 1*s* MARPE from Mn and Fe oxides. So far the influence of W_p has been neglected; however, this can play an important role in particular near the resonant energy.

In a previous paper,[7] we demonstrated the importance of the structure factors which are proportional to R^{-3} (R is the metal-O distance). It is thus sufficient to consider only the nearest neighbors. Both of the amplitudes $A(\mathbf{R}_{\alpha},\omega)_{m'}^d$ and $A'(\mathbf{R}_{\alpha},\omega)_{m'}^d$ are proportional to $y_{10,1m'}(\mathbf{R}_{\alpha},\omega)$ defined by Eqs. (25) and (26). A "selection rule" of the MARPE is obtained by checking the sum over the first shell sites

$$\sum_{\alpha} y_{10,1m}(\mathbf{R}_{\alpha}) = -\sum_{\alpha}\frac{4\pi}{R_{\alpha}^3}G(2-m1m|1)Y_{2-m}(\hat{\mathbf{R}}_{\alpha}). \quad (35)$$

We can show some local symmetries which make the above sum vanish. When the system has an n-fold rotation axis parallel to $\mathbf{E}(\|z)$ around a photoemitting atom (for example, O in MnO), the operation of n-fold rotation C_n on $Y_{lm}(\hat{\mathbf{R}})$ yields the phase change if $m \neq 0$,

$$C_nY_{lm}(\hat{\mathbf{R}}) = e^{im\Phi}Y_{lm}(\hat{\mathbf{R}}), \quad \Phi = \frac{2\pi}{n}. \quad (36)$$

We thus have the relation by noting that $\hat{\mathbf{R}}_p = C_n^{-p}\mathbf{R}$

$$\sum_{p=0}^{n-1}Y_{lm}(\hat{\mathbf{R}}_p) = \sum_{p=0}^{n-1}C_n^pY_{lm}(\hat{\mathbf{R}}) = \sum_{p=0}^{n-1}e^{imp\Phi}Y_{lm}(\hat{\mathbf{R}}) = 0 \quad (m=\pm1), \quad (37)$$

from which we have for these highly symmetric cases

$$\sum_{\alpha} y_{10,1\pm1}(\mathbf{R}_{\alpha}) = 0. \quad (38)$$

In this paper we also study more detailed conditions to observe finite MARPE spectra.

A. O_h and related structure

Figures 2(a)–2(d) show three typical local structures related to O_h symmetry. First, we calculate the sum (35) in the structure factor for the simplest model, "MnO bulk (octahe-

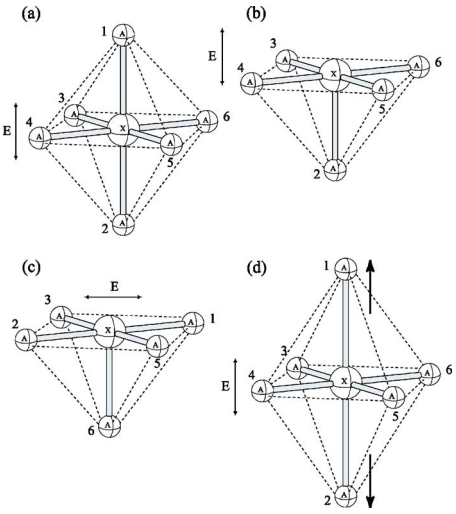

FIG. 2. (Color online) O_h structure (a) and lower symmetric structures, surface models (b) and (c), and distorted model (d). The central atom is the photoemitting oxygen atom and five or six metal atoms are surrounding it. In (b) the x-ray polarization is normal to the surface, whereas in (c) it is parallel to the surface.

dral) model," where six Mn atoms occupy octahedral sites around the O atom shown by Fig. 2(a). As discussed, we assume the linear polarization in the z direction. For this high symmetric coordination we have

$$\sum_{\alpha=1}^{6} y_{10,1\pm1}(\mathbf{R}_\alpha) = 0. \tag{39}$$

We should note that this detailed cancellation works for all systems with O_h symmetry around an oxygen atom irrespective of the distance R. We thus cannot expect to observe MARPE for this high symmetric system like MnO, NiO crystals, and so on. This result demonstrates that the O 1s MARPE cannot be observed for perfect MnO crystals. This seems inconsistent with the observed results,[9,10] where they have observed prominent MARPE for these systems.

We calculate O 1s MARPE for a "MnO(001) surface model," where a surrounding Mn atom along $+z$ direction is lost [as shown by Fig. 2(b)]. This system is in the lower symmetry than octahedral symmetry, and we have

$$\sum_{\alpha=2}^{6} y_{10,10}(\mathbf{R}_\alpha) = \frac{2}{R^3},$$

$$\sum_{\alpha=2}^{6} y_{10,1\pm1}(\mathbf{R}_\alpha) = 0. \tag{40}$$

The latter relation is easily understood from Eq. (38) because the surface oxygen atoms have four-fold symmetry around the z axis. We thus can have finite MARPE signal from the (001) surface model. From Eqs. (30), (32), and (34), the effective excitation operator Δ'' has only $Y_{10}(\hat{\mathbf{r}})$ as the angular part: The angular dependence of MARPE is the same as that of main photoemission band for these systems.

To study the x-ray polarization dependence, we calculate the MARPE for another model shown by Fig. 2(c), where a Mn atom along $+x$ direction ["4" labeled in Fig. 2(a)] is lost. This model corresponds to the case where the x-ray polarization is parallel to the surface, which gives

$$\sum_{\alpha(\neq4)} y_{10,10}(\mathbf{R}_\alpha) = -\frac{1}{R^3},$$

$$\sum_{\alpha(\neq4)} y_{10,1\pm1}(\mathbf{R}_\alpha) = 0. \tag{41}$$

For the parallel polarization ($\mathbf{E}\|$surface) we expect the smaller MARPE with half strength of that for the normal ($\mathbf{E}\perp$surface) polarization and with quite different shape because of the different sign of the sum. The effective excitation operator Δ'' has only $Y_{10}(\hat{\mathbf{r}})$ as the angular part as before.

As MARPE reflects only nearest-neighbor atomic structure, the surface model shown by Fig. 2(c) can also be considered as a defect model and also a substitution model: For example, one Mn atom is replaced by Ni, where the 2p binding energy is quite different from the Mn 2p energy.

The energy dependence of $f_d(\omega)$ defined by Eq. (14) is directly calculated, whereas $f_d''(\omega)$ defined by Eq. (31) is approximately calculated by use of a rather crude approxima =tion (15)

$$f_d''(\omega) \sim f_d(\omega)\frac{4\pi}{3}\sum_{m_d}\langle\phi_d|\Delta^* g_{sc}(\omega+\varepsilon_d)\tilde{\Delta}|\phi_d\rangle$$

$$= -\frac{2\pi}{3} f_d(\omega)\tilde{f}_d(\omega), \quad \tilde{\Delta} = Y_{10}(\hat{\mathbf{r}})/r^2. \tag{42}$$

We have used $\tilde{f}_d(\omega)$ defined by Eq. (20), which is well approximated by[31]

$$\tilde{f}_d(\omega) = \frac{\gamma}{\omega+\varepsilon_d+i\Gamma_d/2}, \tag{43}$$

where γ is energy parameter and Γ_d is the lifetime broadening of the deep core hole state on d. The parameter γ is approximately given by

$$\gamma = -2\sum_{p}^{vac}\langle\phi_d|\Delta|\phi_p\rangle\langle\phi_p|\tilde{\Delta}|\phi_d\rangle, \tag{44}$$

where the sum over p is taken over vacant one-electron states. For the unoccupied one-electron states, we can safely use single-site approximation because ϕ_d is strongly localized. We can roughly estimate the γ value as -2.2 eV by use of Hartree-Fock atomic orbital, and by taking only 3d holes. In this subsection, we fix Mn-O distance at 2.23 Å and Γ_d =0.5 eV.[11] These approximations yield the photoemission intensity near the MARPE threshold

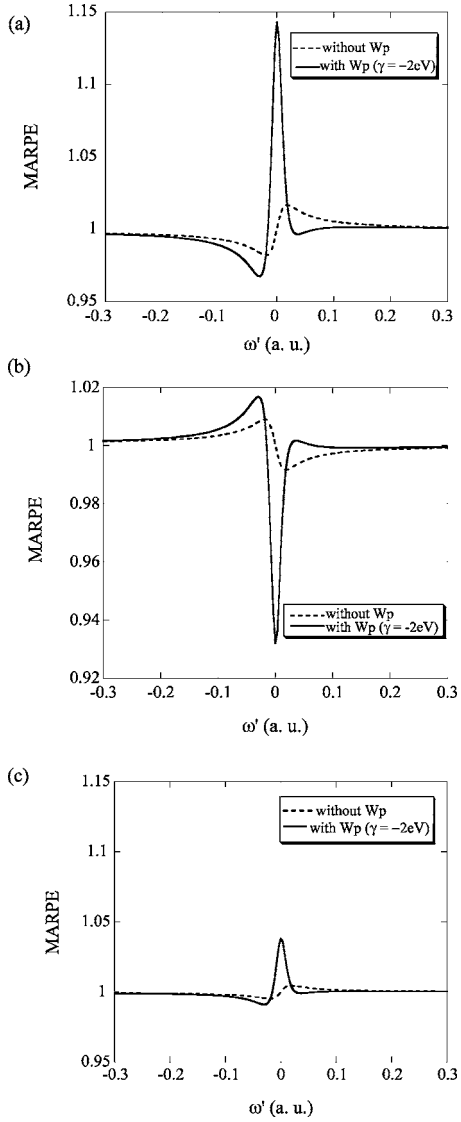

FIG. 3. O 1*s* MARPE near the Mn 2*p* threshold (a) for the surface model shown by Fig. 2(b) ($\mathbf{E}\perp$ surface), (b) for the surface model shown by Fig. 2(c) ($\mathbf{E}\|$surface), and (c) for the distortion model by Fig. 2(d). The calculated MARPE with W_p is much larger than that without W_p. The MARPE is normalized to the atomic photoemission intensity, and we define $\omega' = \omega + \varepsilon_d$.

$$I(\mathbf{p},\omega) \propto \left| \langle f_{\mathbf{p}}^{-} | r Y_{10}(\hat{\mathbf{r}}) | \phi_c \rangle - \frac{2\pi}{3} f_d(\omega) \times \left(1 + \frac{\gamma}{\omega + \varepsilon_d + i\Gamma_d/2} \right) \sum_{m',\alpha} y_{10,1m'}(\mathbf{R}_\alpha) \times \langle f_{\mathbf{p}}^{-} | r Y_{1m'}(\hat{\mathbf{r}}) | \phi_c \rangle \right|^2 . \quad (45)$$

The present MARPE analyses are carried out by use of the approximate formula (45).

At first we study the influence of W_p on MARPE. Figure 3(a) shows the calculated O 1*s* MARPE near the Mn 2*p* threshold for the MnO surface model as shown by Fig. 2(b).

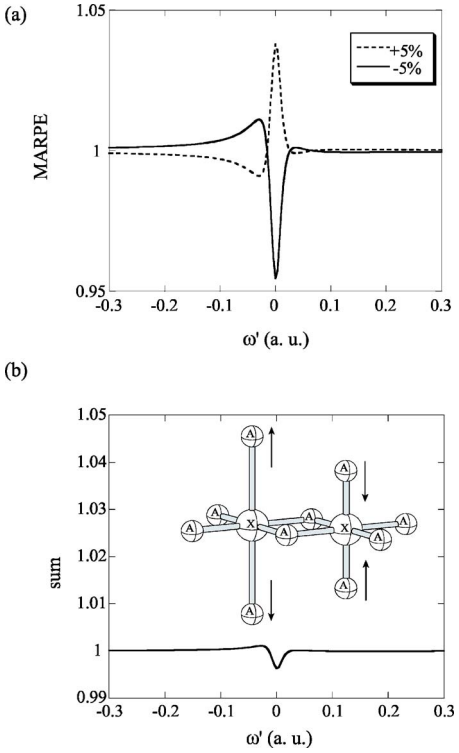

FIG. 4. (Color online) Calculated O 1*s* MARPE spectra (a) for the two distortion models where two Mn atoms on the *z* axis are displaced to have a longer (+5%) and shorter (−5%) Mn-O distance, and (b) for the alternating distortion model where Mn-O distances parallel to the *z* axis are alternatively longer (+5%) and shorter (−5%).

We compare the calculated result without $W_p(\gamma=0)$ where A' is neglected in Eq. (34) with that where both A and A' are taken into account. The former gives weak MARPE whose relative intensity to the main photoemission band is about 2%. In contrast to this result, the latter, including the dynamical polarization, gives a prominent peak comparable with the experimental one (~12%),[10] and still shows a Fano-like asymmetric shape. We have used the parameter $\gamma=-2$ eV to obtain a good agreement with the experimental result. This result is quite close to the rough estimate of γ value described before. We thus find that the dynamical polarization W_p is important to explain quite large MARPE as reported in the literature.[10] Figure 3(b) shows the calculated O 1*s* MARPE for the MnO surface model as shown by Fig. 2(c) ($\mathbf{E}\|x$). As expected from Eq. (41) the MARPE shows a negative peak with smaller intensity (~−7%) in comparison with the normal polarization [Fig. 3(a)]. Figure 3(c) shows the calculated results for the distorted model shown by Fig. 2(d), where there are two Mn atoms on the *z* axis with 5% longer Mn-O distance. This small distortion can give rise to detectable MARPE (~5%), which is still much smaller than that for the surface model. Without W_p the calculated MARPE is much smaller than that with W_p as before. From now on, all calculated MARPE spectra are shown which include W_p.

Figure 4(a) shows the calculated results for the distortion models, where two Mn atoms on the *z* axis have a longer (+5%) and shorter (−5%) Mn-O distance R' than the other

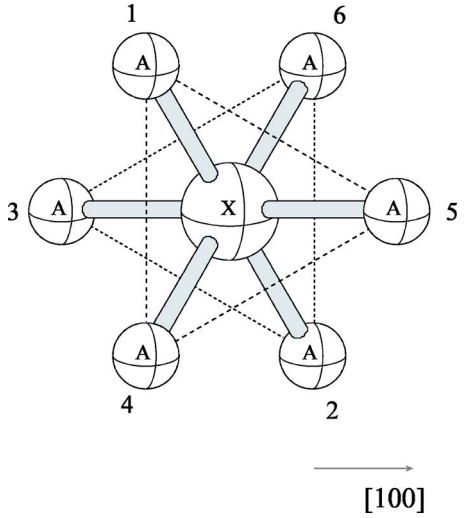

FIG. 5. (Color online) MnO (111) surface structure around an oxygen (X) atom surrounded by six metal atoms (A).

four (in the xy plane) Mn-O distance R. In this case we have

$$\sum_{\alpha=1}^{6} y_{10,10}(\mathbf{R}_\alpha) = 4\left(\frac{1}{R^3} - \frac{1}{R'^3}\right) \sim \frac{12\delta R}{R^4},$$

$$\sum_{\alpha=1}^{6} y_{10,1\pm1}(\mathbf{R}_\alpha) = 0, \tag{46}$$

where $\delta R = R' - R$. If the distortion is small enough, the MARPE for the model $\delta R > 0$ can be obtained by inverting its sign of A and A'. Figure 4(b) shows the calculated O 1s MARPE for a model where two Mn-O distances parallel to the z axis are alternately longer (+5%) and shorter (−5%), as shown in the figure. The MARPE is less than 0.5% because of the imperfect cancellation; the distortion is considerably large. Of course, the alternating distortion is not essential. The same result is obtained for the models where +5% distortion parallel to the z axis and −5% distortion are equally distributed around oxygen atoms.

We should note that the O 1s MARPE for MnO is very surface sensitive, because O 1s photoelectron kinetic energy is ~100 eV at the resonant threshold so that the photoelectron mean free path is quite small. Thus we conclude that O 1s surface photoemission can give rise to prominent MARPE as observed for the MnO (001) surface.

To study the surface dependence of MARPE we calculate the sum (35) for the "MnO (111) model" shown by Fig. 5 where the x-ray polarization is normal to the (111) surface. When an oxygen layer is in the outermost layer, the nearest-neighbor Mn atoms only occupy the sites 2, 3, and 6. In this case we have

$$\sum_{\alpha=2,3,6} y_{10,1m'}(\mathbf{R}_\alpha) = 0 \quad (m' = 0, \pm 1), \tag{47}$$

so that the photoemission from the outermost surface O atoms give no MARPE. When a Mn layer is outermost, six Mn atoms are there in the first shell. We also have

$$\sum_{\alpha=1,4,5} y_{10,1m'}(\mathbf{R}_\alpha) = 0 \quad (m' = 0, \pm 1), \tag{48}$$

thus the surface O atoms in the second layer also give no MARPE as expected. We cannot expect to observe MARPE both for O-terminated and Mn-terminated surfaces. According to Ref. 32, reconstructed MnO (111) thin-film surfaces have a different Mn-O distance in each layer. In this case the sum (47) or (48) never vanishes for $m' = 0$, and we can expect finite MARPE which have the same order of the distortion model. If there are some defects or substitution near the surface region, MARPE can be observed as discussed, without changing the Mn-O distance.

B. CsCl and T_d structure

Let us consider other local structures such as CsCl and T_d structures. Though bulk MnO cannot have these symmetries, we try to stress the importance of local symmetry on MARPE. We thus assume such structures of MnO for the MARPE calculations: the Mn-O distance is assumed to be 2.23 Å as before.

For the CsCl structures shown in Fig. 6(a), the sum (35) vanishes irrespective of x-ray polarization $\mathbf{E} \| [001]$ or $\mathbf{E} \| [111]$, so that O 1s MARPE should also disappear. On the other hand, the surface photoemission can give finite MARPE structures, which depend on the surface planes. For the oxygen-terminated (001) surface model where four nearest-neighbor Mn atoms in the upper layer are lost, the sum (35) vanishes even for this low symmetric structure; each surface oxygen has a fourfold axis so that the sum (35) vanishes when $m' = \pm 1$. The sum also vanishes even for $m' = 0$ since $\cos\theta_\alpha = -1/\sqrt{3}$. On the other hand, the Mn-terminated (111) surface model has a threefold axial symmetry which makes the sum null if $m' \neq 0$. For the case $m' = 0$ we can expect finite MAPRE since the sum (35) gives the same result as shown by Eq. (40) for the MnO (001) surface.

We next study the MARPE from tetrahedral structures shown by Fig. 6(c); CuCl and the wurtzite (ZnO) structure have this local symmetry around an oxygen atom. When the x-ray polarization is parallel to one of the Mn-O bonds as shown by Fig. 6(c), the sum (35) vanishes for all $m'(=0, \pm 1)$. That is also the case when the x-ray polarization direction ($\| z'$) is parallel to the twofold axis which bisects the angle between two neighboring Mn-O bonds. We cannot observe MARPE for crystals with T_d symmetry. In contrast to these results, the surface model where one Mn atom labeled 1 is lost gives finite MARPE, since we have for the x-ray polarization ($\mathbf{E} \| z$)

$$\sum_{\alpha=2,3,4} y_{10,10}(\mathbf{R}_\alpha) = \frac{2}{R^3}. \tag{49}$$

On the other hand, when the x-ray polarization is parallel to the z' axis and the surface plane is normal to the z' axis, we cannot expect finite MARPE both for Mn and O outermost layers.

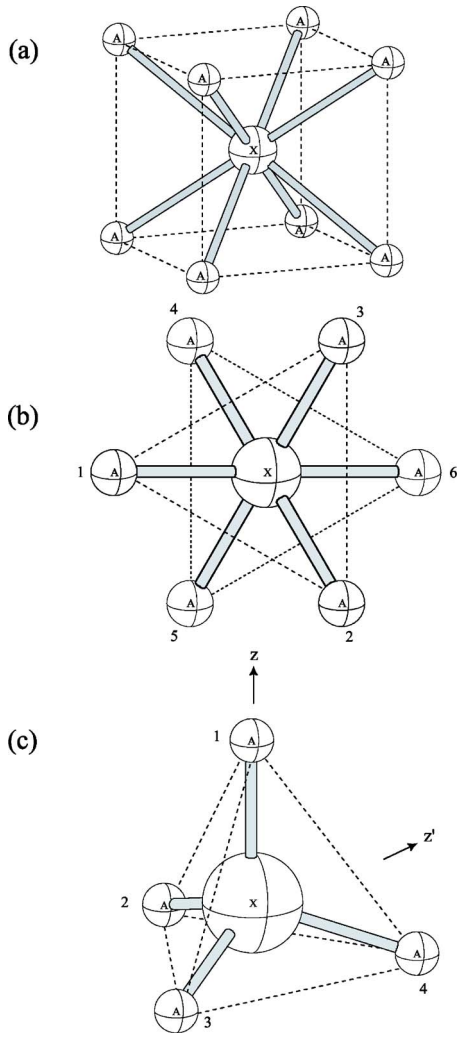

FIG. 6. (Color online) Two local structures: (a) the CsCl bulk model and (b) the CsCl (111) surface model where 1, 2, and 3 are the metal atoms in the top layer, and 4, 5, and 6 in the third layer. An atom labeled by 7 exists below the emitter *X*. (c) Tetrahedral structure for the two different x-ray polarizations, $\|z$ and $\|z'$.

C. Rutile, perovskite, and α-alumina structures

In this section we study MARPE from lower symmetric systems like rutile, perovskite, and α-alumina structures. First we consider MnO_2 as an example of the rutile structure shown by Fig. 7(a). Oxygen and Mn atoms are shown by large and small spheres. Two Mn-O bonds are a little shorter (1.88 Å) than another Mn-O bond (1.95 Å). The x-ray polarization direction is parallel to z axis shown in the figure. Outermost surface oxygen atoms are labeled 1 and 2, and oxygen atoms labeled 3 and 4 are in the second layer, and 5 and 6 are in the third layer. These oxygen atoms in the second and the third layers have three nearby Mn atoms as described earlier, whereas the outermost surface oxygen atoms have only two Mn atoms. In this structure, oxygens 1 and 2 give the same MARPE signal shown by the solid line with circles in Fig. 7(b). The inner oxygens 3–6 also give the finite MAPRE whose intensity and sign are different from the surface MARPE as shown by the broken line in Fig. 7(b):

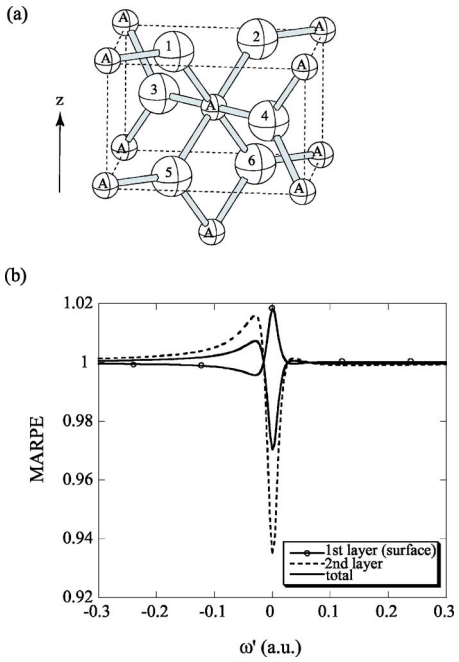

FIG. 7. (Color online) (a) MnO_2 rutile structure is shown where oxygen atoms are shown by large spheres labeled 1–6 and Mn by small spheres "A." (b) Calculated O 1*s* MARPE spectra from MnO_2 near Mn 2*p* threshold. The MARPE from the outermost surface (atoms 1 and 2) and the second layer (atoms 3 and 4) are shown, and compared with the total in the normal emission mode [see Eq. (50)].

the MARPE from the second, third, etc. layers are the same as far as we neglect photoelectron diffraction. In these calculations the sum (35) except $m'=0$ vanishes both for the first and second layers. The photoemission intensities from the inner layers decrease because of the photoelectron damping effect. Thus the total MARPE intensity $I(\omega)$ is obtained for the normal emission

$$I(\omega) = I_1(\omega) + I_2(\omega)e^{-d/\lambda} + I_3(\omega)e^{-2d/\lambda} + \cdots$$
$$= I_1(\omega) + I_2(\omega)\frac{1}{e^{d/\lambda} - 1}, \quad (50)$$

where I_i means the photoemission intensity from the ith layer without the damping and the photoelectron diffraction from the surrounding atoms, d is the interlayer distance, and λ is the mean free path of the photoelectrons. If we measure the photoelectron current at the tilt angle θ_p, then d should be replaced by the propagated distance $d'=d/\cos\theta_p$. For this surface, all inner oxygen atoms give the same MARPE, so we can put $I_2(\omega)=I_3(\omega)=\cdots$. Because O 1*s* photoelectron kinetic energy near Mn 2*p* threshold is about 100 eV, we have quite a short mean free path ($\lambda \sim 4$ Å). The solid line in Fig. 7(b) shows the total MARPE intensity calculated by Eq. (50), which is quite similar to that from the second layer. In this case the MARPE is not so surface sensitive. Of course we can change the surface sensitivity by controlling θ_p; the surface MARPE dominantly contributes to the total for small θ_p.

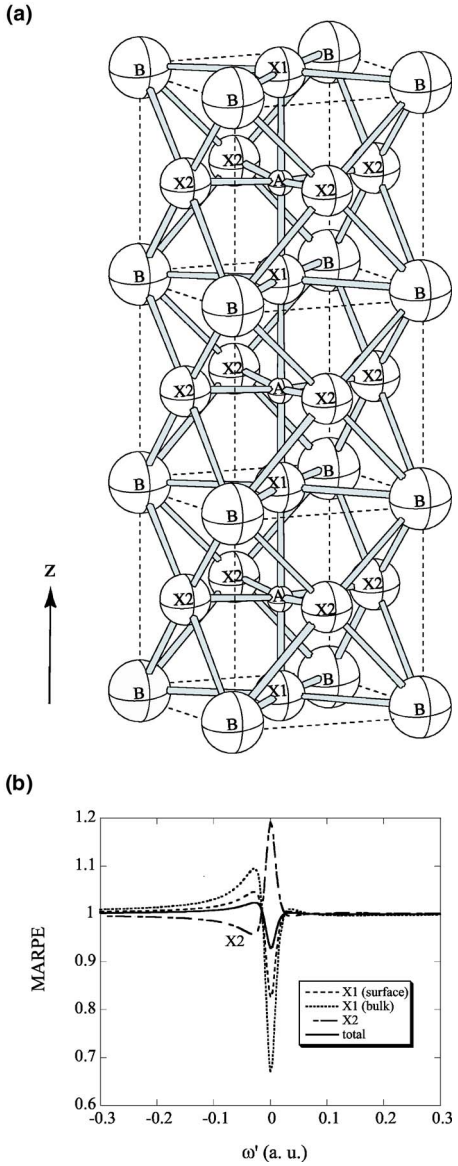

FIG. 8. (Color online) (a) Perovskite structure. For $BaTiO_3$, A and B are Ti and Ba sites, and X is O. We have two different bulk local site of O shown by $X1$ and $X2$: The outermost $X1$ is in different local symmetry from the bulk $X1$. (b) Calculated O $1s$ MARPE spectra from oxygen atoms in different layers. The total means the weighted sum of the photoemission band from each layer [see Eq. (53)].

Now let us consider a perovskite structure shown by Fig. 8(a); a well-known example is $BaTiO_3$ (Ti is at the A site, Ba at the B site, and O at the X site). Bulk $X1$ oxygen atoms have two nearby resonant atoms labeled by A along the z axis, and we have the sum over resonant atoms A (B atoms have no contribution to the MARPE),

$$\sum_{\alpha\in A} y_{10,10}(\mathbf{R}_\alpha) = -\frac{4}{R^3}, \quad \sum_{\alpha\in A} y_{10,1\pm1}(\mathbf{R}_\alpha) = 0, \qquad (51)$$

for bulk $X1$. In this case the photoemission from the second, third, etc. layers gives rise to the same MARPE. In the outermost surface layer, one $X1$ oxygen has one resonant atom A, which has half a contribution to the structure factor in comparison with the bulk $X1$ oxygen. On the other hand, one $X2$ oxygen atom has two resonant atoms A in the plane normal to the z axis and

$$\sum_{\alpha\in A} y_{10,10}(\mathbf{R}_\alpha) = \frac{2}{R^3}, \quad \sum_{\alpha\in A} y_{10,1\pm1}(\mathbf{R}_\alpha) = 0 \qquad (52)$$

for bulk $X2$. The total MARPE is obtained by summing up all the photoemission intensities as before. Here $I(X1)$ is the photoemission intensity from inner $X1$ site and $I(\text{surface};X1)$ is that from the outermost $X1$ site. We have the total photoemission intensity I as the sum for the normal emission

$$I = I(\text{surface};X1) + 2I(X2)e^{-d/\lambda} + I(X1)e^{-2d/\lambda} + \cdots$$
$$= I(\text{surface};X1) + \{I(X1) + 2I(X2)e^{d/\lambda}\}\frac{1}{e^{2d/\lambda}-1}, \qquad (53)$$

where d is half of the nearest $X1$-$X1$ distance. As the Ti $2p$ threshold is lower than O $1s$ ionization energy, we cannot expect O $1s$ MARPE near the Ti $2p$ threshold. As discussed, however, we can expect finite O $1s$ MARPE from perovskite structure as long as all Ti are substituted by Fe, Mn, …. Figure 8(b) shows the calculated O $1s$ MARPE from the perovskite "$BaMnO_3$" where the Mn-O the distance is assumed to be the same as that in $BaTiO_3$ (2.03 Å). The MARPE from the outermost surface layer oxygen shown by a broken line is about half of that from the bulk $X1$ oxygen atoms shown by a dotted line. The calculated O $1s$ MARPE from $X2$ oxygen atoms $I(X2)$ shown by a dashed-dotted line has a different sign but almost the same intensity in magnitude as that from a bulk $X1$ oxygen. A solid line shows the total MARPE calculated from Eq. (53), where we have used $\lambda \sim 4$ Å. The MARPE from a bulk $X1$ oxygen amounts to 30%, which is cancelled by the MARPE from an $X2$ oxygen. The total MARPE is still large enough, ~10%.

Next let us consider Fe_2O_3 as an example of an α-alumina structure. Figure 9(a) shows the α-alumina structure where 1, 2, and 3 are in the first oxygen layer, and 4, 5, and 6 are in the second. They all have different local symmetries. The Fe-O distance is smaller than Mn-O; the two shorter Fe-O bond distances are 1.86 Å and the two longer bond distances 1.97 Å. We consider all of the four Fe atoms for the MARPE calculation since their bond lengths are not so different. We assume for simplicity the same values of Γ_d and γ in Eq. (43) as used for the Mn-O system. Near the resonant energy, the photoelectron kinetic energy is 170 eV, and the mean free path is a little larger than that in MnO. In Fig. 9(b) "surface" shows the averaged MARPE from the surface oxygen atoms (1, 2, and 3), which have only two Fe neighbors. The calculated MARPE from the second layer, which is averaged over the MAPRE from 4, 5, and 6 with the same weight, is also shown by "bulk." Both of the MARPE are quite similar. From symmetric consideration we can expect that the MARPE from the second and third layers have the same shape. We can thus calculate the total intensity by use of Eq. (50). As observed for the rutile and the perovskite structures, the α-alumina structure (Fe_2O_3) also gives MARPE in both

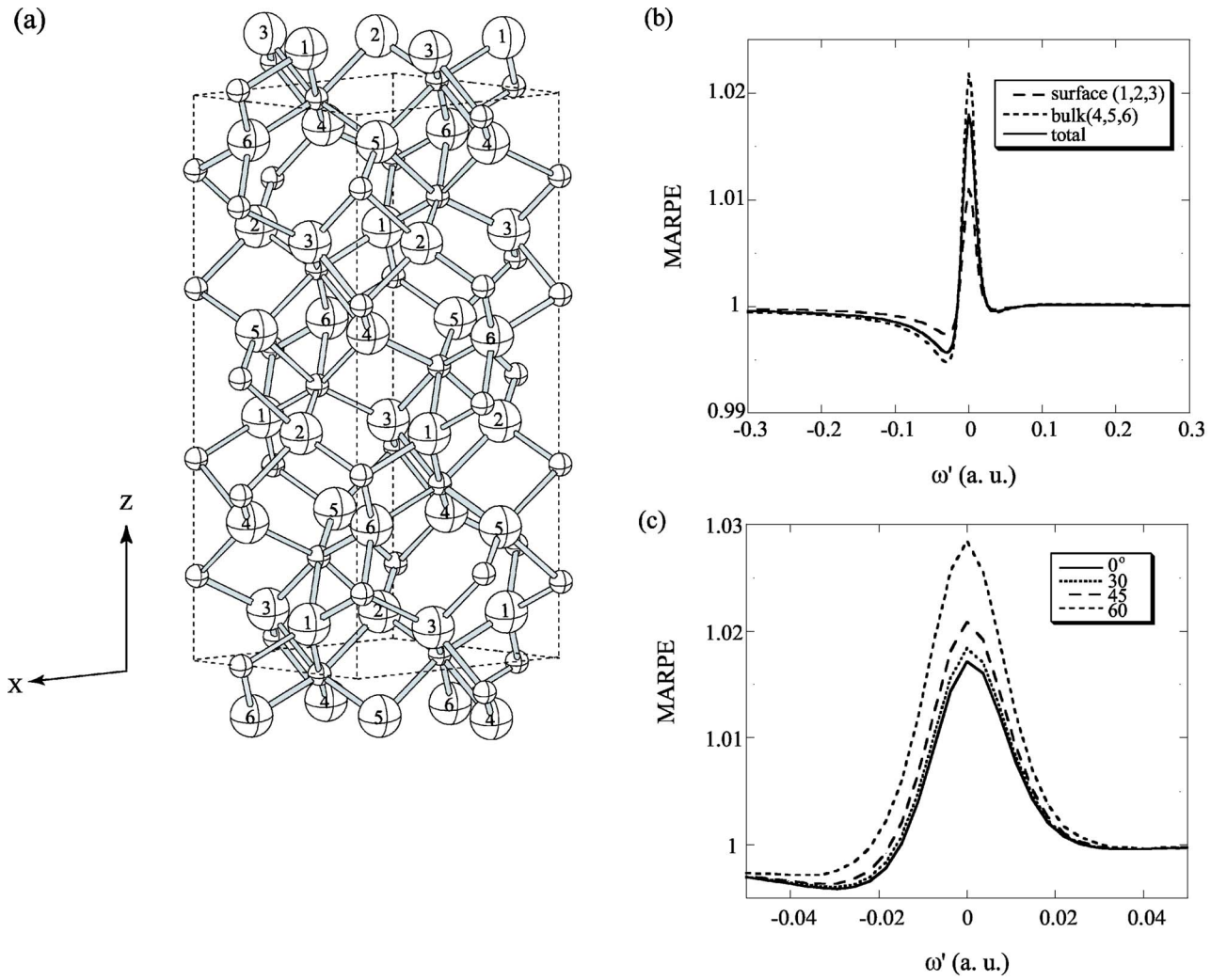

FIG. 9. (Color online) (a) α-alumina structure. Outermost oxygen atoms are labeled by 1, 2, and 3; second-layer oxygen atoms by 4, 5, and 6. In the outermost surface layer there are three different types of oxygen atoms where the ratio is 1:1:1. They all have two adjacent iron atoms in comparison to inner oxygen atoms surrounded by four iron atoms. In the second layer there are three different types of oxygen atoms—4, 5, and 6—with the same ratio. That is also the case for each inner layer. (b) Calculated normal emission O 1*s* MARPE spectra from Fe_2O_3 with α-alumina structure. The broken line and the dotted line show the calculated results for the "surface" (outermost) and "bulk" (second) layers, respectively. Both the outermost and the second-layer oxygen atoms give observable MARPE. The solid line shows calculation results with the damping effects. (c) Calculated angle-resolved O 1*s* MARPE spectra normalized to the nonresonant photoemission intensity neglecting $A_m(m=0,\pm1)$ in Eq. (54). The results are shown for θ_p=0, 30, 45, and 60°.

surface and inner layer photoemission. In this case the sum (35) for $m'=\pm1$ does not vanish as well as for $m'=0$, and the photoemission intensity is given by

$$I(\mathbf{p},\omega) \propto |(1+A_0(\omega))\langle f_{\mathbf{p}}^-|rY_{10}|\phi_c\rangle + A_1(\omega)\langle f_{\mathbf{p}}^-|rY_{11}|\phi_c\rangle + A_{-1}(\omega)\langle f_{\mathbf{p}}^-|rY_{1-1}|\phi_c\rangle|^2, \quad (54)$$

where in terms of A_m^d and $A_m'^d$ defined Eqs. (25) and (26)

$$A_m(\omega) = \sum_\alpha [A(\mathbf{R}_\alpha,\omega)_m^d + A'(\mathbf{R}_\alpha,\omega)_m^d]. \quad (55)$$

In contrast to all of the previous results, the spectral shape is expected to be angular dependent. Figure 9(c) shows the calculated O 1*s* MARPE for different detection angle θ_p measured from the z axis, where we fix azimuthal angle ϕ_p =0($\|x$). The spectra are normalized to the nonresonant photoemission intensity at the same detection position. The second and the third terms in Eq. (54) are caused by the resonant interaction. For the large polar angle θ_p, the resonant effect is enhanced in the second and the third terms because of the sin θ_p dependence. The first term has cos θ_p angular dependence which should be smaller than the other resonant terms at large θ_p. This is the reason why the MARPE is large for large θ_p. Since the energy dependence of $A_{\pm1}(\omega)$ is different from that of $A_0(\omega)$, the MARPE shape can be dependent on θ_p. The calculated MARPE shape, however, is not so sensitive to θ_p. The calculated MARPE from Fe_2O_3 is much smaller than the observed one[9] which neglected detector nonlinearity,[14] so that a detailed comparison is impossible. Although MnO MARPE is very surface sensitive, O 1*s* MARPE for Fe_2O_3 is not surface sensitive because of the

TABLE I. Theoretical prediction to measure MARPE for various systems. The symbols × and ◯ show the null and finite MARPE. In particular, "strong" shows the intense MARPE larger than 10%.

Structure	Inner layer	Outermost layer
octahedral (001)	×	strong
octahedral (111)	×	×
octahedral (111) reconst.	×	◯
tetrahedral	×	◯
CsCl (001)	×	×
CsCl (111)	×	◯
rutile (001)	◯	◯
perovskite (001)	strong	◯
α-alumina (001)	◯	◯

large mean free path for higher kinetic energy in addition to the finite MARPE even from inner layers.

IV. CONCLUSION

We have found that the condition to observe MARPE is strongly influenced by the "structure factor," which reflects the local symmetry around an emitting atom. We studied the structure factor for some simple model clusters and the influence of the polarization part W_p of screened Coulomb interaction $W(\omega)$ on MARPE. Finally, Table I summarizes the calculated results for some bulk and surface systems where ◯ and × show finite and null MARPE to be observed. In particular, "strong" means the intense MARPE larger than 10%. The difference of a resonant atom such as Mn and Fe is not essential to observe finite MARPE, but the structure factor plays a crucial role and is sensitive to the symmetry around the emitter. This is one of the conditions to observe MARPE. Photoelectron kinetic energy is also important; for example, the surface-sensitive MARPE from the MnO (001) surface should be larger than that from NiO ($\varepsilon_{\mathbf{k}} \sim 340$ eV).

For a detailed comparison, we should include the photoelectron diffraction effects.[33–38] These effects can give some fine structures on the overall resonant shape.

We successfully related the resonant terms both in on-site and multisite resonant photoemission to the x-ray absorption factor $f_d(\omega)$ from the deep core ϕ_d, which has been used in the analyses of the resonant x-ray scattering. These resonant terms arise from the radiation field screening, which is essential for the MARPE analyses. On the other hand, the vertex correction shown by Figs. 1(b)–1(d) also plays an important role in the analyses of on-site resonant photoemission spectra. We should note that W_p also plays an important role in other resonant phenomena accompanied by core excitations, although it is of the second-order. The importance of the second order term in the analyses of resonant photoemission has been pointed out from a different theoretical approach.[27] In the present treatment, the radiation field is taken into account as external perturbation. A quantum electrodynamics (QED) Keldysh Green's function approach allows to renormalize photon field in the photon Green's functions and to calculate the radiation field screening in a natural way.[39]

ACKNOWLEDGMENTS

The author (H. A.) is grateful for financial support from 21 COE program (Frontiers of Super Functionality Organic Devices). The author (T. F.) is grateful for financial support from a Grant-in-Aid for Scientific Research from the Ministry of Education, Science and Culture of Japan (No. 13640318).

APPENDIX A: EQUATION OF MOTION OF $f_{\mathbf{p}}^{-}(1)$

So far no detailed formal discussion has been given on the optical potential working on $f_{\mathbf{p}}^{-}$. Here we show that advanced self-energy $\Sigma^a(\varepsilon_p)$ plays an optical potential for $f_{\mathbf{p}}^{-}$.

The photoelectron Dyson orbital $f_{\mathbf{p}}^{-}(1)$ is defined as Eq. (2.11) in Ref. 7, which is also written as

$$f_{\mathbf{p}}^{-}(1) = \langle 0|\psi(1)|0,\mathbf{p}^{-}\rangle = \langle 0|\psi(x_1)|0,\mathbf{p}^{-}\rangle e^{-i\varepsilon_p t_1}, \quad \text{(A1)}$$

where the scattering state $|0,\mathbf{p}^{-}\rangle$ is related to the target state $|0\rangle$ (Refs. 40 and 41)

$$|0,\mathbf{p}^{-}\rangle = \eta \int_0^\infty d2\, \phi_{\mathbf{p}}^{-}(2)\psi^\dagger(2)|0\rangle \equiv L_{\mathbf{p}}^{-}(2)\psi^\dagger(2)|0\rangle \quad (\eta \to +0). \quad \text{(A2)}$$

We define the outgoing scattering wave function $\phi_{\mathbf{p}}^{-}(2)$ for the Hartree-Fock potential V as

$$\phi_{\mathbf{p}}^{-}(2) = \phi_{\mathbf{p}}^{-}(x_2)e^{-i(\varepsilon_p - i\eta)t_2}. \quad \text{(A3)}$$

We find that the integral operator $L_{\mathbf{p}}^{-}(2)$ satisfies

$$L_{\mathbf{p}}^{-}(2)\langle 0|\psi^\dagger(2) = 0,$$

since the ground state $|0\rangle$ has no scattering component. From these $f_{\mathbf{p}}^{-}$ is given by

$$\begin{aligned} f_{\mathbf{p}}^{-}(x_1) &= L_{\mathbf{p}}^{-}(2)\langle 0|\psi(x_1)\psi^\dagger(2)|0\rangle = L_{\mathbf{p}}^{-}(2)\langle 0|\{\psi(x_1),\psi^\dagger(2)\}|0\rangle \\ &= L_{\mathbf{p}}^{-}(2)\,\theta(t_2)\langle 0|\{\psi(x_1),\psi^\dagger(2)\}|0\rangle \\ &= -iL_{\mathbf{p}}^{-}(2)g^a(1,2) \quad (t_1 \to -0), \end{aligned} \quad \text{(A4)}$$

where the advanced Green's function g^a,

$$ig^a(1,2) = -\theta(t_2 - t_1)\langle\{\psi(1),\psi^\dagger(2)\}\rangle, \quad \text{(A5)}$$

is introduced. As observed for the retarded Green's function $g^r(g^r = g_0^r + g_0^r\Sigma^r g^r)$, g^a also satisfies the closed Dyson equation

$$g^a = g_0^a + g_0^a\Sigma^a g^a. \quad \text{(A6)}$$

From Eqs. (A4) and (A6) we have an equation for $f_{\mathbf{p}}^{-}$

$$f_{\mathbf{p}}^{-}(x_1) = \phi_{\mathbf{p}}^{-}(x_1) + \int dx_2 dx_3\, g_0^a(x_1,x_3;\varepsilon_p)\Sigma^a(x_3,x_2;\varepsilon_p)f_{\mathbf{p}}^{-}(x_2). \quad \text{(A7)}$$

We can rewrite this equation by noting that

$$\hat{h}(x_1)\phi_{\mathbf{p}}^{-}(x_1) = \varepsilon_p \phi_{\mathbf{p}}^{-}(x_1), \tag{A8}$$

where $\hat{h}$ is one-electron Hamiltonian given by $\hat{h}=h+V$ (V is the Hartree-Fock potential and $h=T_e+V_{en}$). Let us operate $\hat{h}(x_1)$ on the both sides of Eq. (A7). From Eq. (A8) and

$$[\varepsilon_p - \hat{h}(x_1)]g_0^a(x_1,x_2) = \delta(x_1 - x_2),$$

we obtain an integro-differential equation

$$\begin{aligned}\hat{h}(x_1)f_{\mathbf{p}}^{-}(x_1) &+ \int dx_2\, \Sigma^a(x_1,x_2;\varepsilon_p)f_{\mathbf{p}}^{-}(x_2) \\ &= \varepsilon_p\left[\phi_{\mathbf{p}}^{-}(x_1) + \int dx_2 dx_3 g_0^a(x_1,x_3;\varepsilon_p)\Sigma^a(x_3,x_2;\varepsilon_p)f_{\mathbf{p}}^{-}(x_2)\right] \\ &= \varepsilon_p f_{\mathbf{p}}^{-}(x_1).\end{aligned} \tag{A9}$$

This demonstrates that the photoelectron wave function $f_{\mathbf{p}}^{-}$ damps under the influence of the potential $V+\Sigma^a$; the latter depends on the kinetic energy of the photoelectrons. In the GW approximation, the self-energy Σ^a is given by

$$\begin{aligned}\Sigma^a(x,x';\omega) \approx &\sum_{qm} \frac{f_q(x)f_q(x')^* v_m(x')v_m(x)^*}{\omega - \omega_m - \varepsilon_p - i\eta} \\ &+ \sum_{nm} \frac{g_n(x)g_n(x')^* v_m(x')v_m(x)^*}{\omega + \omega_m - \varepsilon_n - i\eta},\end{aligned} \tag{A10}$$

where v_m is a bosonic excitation operator defined by

$$v_m(x) = \int v(\mathbf{r}-\mathbf{r}')\langle m|\psi^\dagger(x')\psi(x')|0\rangle dx'. \tag{A11}$$

In the above derivation we first note that Σ^a is given by

$$\begin{aligned}\Sigma^a(1,2) &= ip_1\theta(t_2-t_1)\{g^>(1,2)W^<(2,1) - g^<(1,2)W^>(2,1)\} \\ &= i\theta(t_2-t_1)\{g^>(1,2)W^<(2,1) + g^<(1,2)W^>(2,1)\}\end{aligned} \tag{A12}$$

in the GW approximation. The Fourier transform of Σ^a is written in terms of $g^>(\varepsilon)$, $g^<(\varepsilon)$, $W^>(\varepsilon')$, and $W^<(\varepsilon')$,

$$\begin{aligned}\Sigma^a(x,x';\omega) = \int \frac{d\varepsilon}{2\pi}\frac{d\varepsilon'}{2\pi}\frac{1}{\omega-\varepsilon+\varepsilon'-i\eta} \\ \times\{g^>(x,x';\varepsilon)W^<(x',x;\varepsilon') \\ + g^<(x,x';\varepsilon)W^>(x',x;\varepsilon')\}.\end{aligned} \tag{A13}$$

The spectral representation of $g^<$ and $g^>$ are given in terms of hole Dyson orbitals $\{g_n\}$ and particle Dyson orbitals $\{f_q\}$[5]

$$g^<(x,x';\varepsilon) = 2\pi i\sum_n g_n(x)g_n^*(x')\delta(\varepsilon-\varepsilon_n), \tag{A14}$$

$$g^>(x,x';\varepsilon) = -2\pi i\sum_q f_q(x)f_q^*(x')\delta(\varepsilon-\varepsilon_q). \tag{A15}$$

Substitution of Eqs. (A14) and (A15), and also of $W^>$ and $W^<$ into Eq. (A13), which are explicitly represented by use of v_m,

$$W^>(x',x;\varepsilon) = -2\pi i\sum_m v_m(x')v_m^*(x)\delta(\varepsilon-\omega_m), \tag{A16}$$

$$W^<(x',x;\varepsilon) = 2\pi i\sum_m v_m^*(x')v_m(x)\delta(\varepsilon+\omega_m), \tag{A17}$$

directly yields Eq. (A10).

This formula can be compared with the previous result.[41,42] In the same way we can obtain an explicit formula of Σ^r.

APPENDIX B: DERIVATION OF EQS. (23)–(29)

We briefly show the derivation of Eqs. (23)–(29). The left-hand side of Eq. (23) is also written as Eq. (8) in terms of g_{sc}^α: we should note that the main contribution to g_{sc} arises from g_{sc}^α but not g_{sc}^A, because $\mathbf{r}_2$, $\mathbf{r}_3$ are localized in the αth atomic region.

$$\begin{aligned}(23) = \sum_{m_d}\int f_{\mathbf{p}}^{-}(\mathbf{r}_1)^*\phi_d(\mathbf{r}_2)^*\frac{1}{|\mathbf{r}_1-\mathbf{r}_2|}\phi_c(\mathbf{r}_1) \\ \times g_{sc}^\alpha(\mathbf{r}_2,\mathbf{r}_3;\omega+\varepsilon_d)\Delta(\mathbf{r}_3)\phi_d(\mathbf{r}_3)d\mathbf{r}_1 d\mathbf{r}_2 d\mathbf{r}_3.\end{aligned} \tag{B1}$$

As $\mathbf{r}_1\in A$, $\mathbf{r}_2$, $\mathbf{r}_3\in\alpha$, the relation $|\mathbf{r}_1-\mathbf{R}_\alpha|>|\mathbf{r}_2-\mathbf{R}_\alpha|$ is always satisfied (we set $\mathbf{R}_A=\mathbf{0}$). In the integrand in (B1), we thus have by use of $\mathbf{r}_2'=\mathbf{r}_2-\mathbf{R}_\alpha$ and $\mathbf{r}_1'=\mathbf{r}_1-\mathbf{R}_\alpha$,[26]

$$\begin{aligned}\frac{1}{|\mathbf{r}_1-\mathbf{r}_2|} &= \sum_{L_1}\frac{4\pi}{2l_1+1}\frac{(r_2')^{l_1}}{(r_1')^{l_1+1}}Y_{L_1}(\hat{\mathbf{r}}_1')Y_{L_1}^*(\hat{\mathbf{r}}_2') \\ &= \sum_{L_1L_2}\frac{4\pi}{2l_1+1}y_{L_1L_2}(\mathbf{R}_\alpha)(r_1)^{l_2}Y_{L_2}(\hat{\mathbf{r}}_1)(r_2)^{l_1}Y_{L_1}^*(\hat{\mathbf{r}}_2),\end{aligned} \tag{B2}$$

where $y_{L_1L_2}(\mathbf{R})$ is defined by Eq. (27). Substitution of Eq. (B2) into Eq. (B1) yields

$$\begin{aligned}(23) = \sum_{Lm_d}\sum_{L_1L_2}\frac{4\pi}{2l_1+1}y_{L_1L_2}(\mathbf{R}_\alpha)\langle f_{\mathbf{p}}^{-}|r^{l_2}Y_{L_2}(\hat{\mathbf{r}})|\phi_c\rangle \\ \times\int R_{l_d}(r_2)g_l^\alpha(r_2,r_3;\omega+\varepsilon_d)R_{l_d}(r_3)r_2^{l_1+2}r_3^3 dr_3 \\ \times G(L_dL_1|L)G(L_d10|L).\end{aligned} \tag{B3}$$

As $y_{L_1L_2}(\mathbf{R}_\alpha)$ behaves as $R_\alpha^{-(l_1+l_2+1)}$ from Eq. (27), we should look for the minimum of the sum l_1+l_2. For the smallest $l_2=0$, however, we have $\langle f_{\mathbf{p}}^{-}|\phi_c\rangle=0$ in Eq. (B3). From the relation

$$\sum_{m_dm}\langle L_dL|10\rangle\langle L_dL|L_1\rangle = \delta_{l_11}\delta_{m_10}, \tag{B4}$$

the lowest term thus has to be $l_1=l_2=1$;

$$\begin{aligned}(23) \sim \frac{4\pi}{3}\sum_l\sum_{m_1m_2}y_{1m_1,1m_2}(\mathbf{R}_\alpha)\langle f_{\mathbf{p}}^{-}|rY_{1m_2}(\hat{\mathbf{r}})|\phi_c\rangle \\ \times\hat{\rho}^\alpha(\omega+\varepsilon_d)_l\sum_{m_dm}G(L_d10|L)G(L_d1m_1|L).\end{aligned} \tag{B5}$$

The sum over m_d and m restricts the m_1 value to $m_1=0$. Finally we obtain the right-hand side of Eqs. (23) and (25).

In the same way we can derive Eqs. (24) and (26).

$$(24) \approx \sum_{sj} \frac{\langle f_{\mathbf{p}}^- g_j | v P_0 v | \phi_c f_s \rangle \langle f_s | \Delta | g_j \rangle}{\omega + \varepsilon_j - \varepsilon_s + i\eta}$$

$$\approx \sum_{m_d} \int f_{\mathbf{p}}^-(\mathbf{r}_1)^* \phi_d^*(\mathbf{r}_2)(vP_0v)(\mathbf{r}_1,\mathbf{r}_2)\phi_c(\mathbf{r}_1) \times g_{sc}^{\alpha}(\mathbf{r}_2,\mathbf{r}_3;\omega+\varepsilon_d)\Delta(\mathbf{r}_3)\phi_d(\mathbf{r}_3)d\mathbf{r}_1 d\mathbf{r}_2 d\mathbf{r}_3. \tag{B6}$$

First we integrate over $\mathbf{r}_3$, which gives

$$\int g_{sc}^{\alpha}(\mathbf{r}_2,\mathbf{r}_3;\omega+\varepsilon_d)\Delta(\mathbf{r}_3)\phi_d(\mathbf{r}_3)d\mathbf{r}_3 = \sum_L \int g_l^{\alpha}(r_2,r_3;\omega+\varepsilon_d)R_{l_d}(r_3)r_3^3 dr_3 G(L_dL|10)Y_L^*(\hat{\mathbf{r}}_2). \tag{B7}$$

As $(vP_0v)(\mathbf{r}_1,\mathbf{r}_2)$ is approximately written in terms of g_{sc}^{α}

$$(vP_0v)(\mathbf{r}_1,\mathbf{r}_2) = \sum_m \int d\mathbf{r}_4 d\mathbf{r}_5 v(\mathbf{r}_1-\mathbf{r}_4)g_m^*(\mathbf{r}_4) \times g_{sc}^{\alpha}(\mathbf{r}_4,\mathbf{r}_5;\omega+\varepsilon_m)g_m(\mathbf{r}_5)v(\mathbf{r}_5-\mathbf{r}_2). \tag{B8}$$

As $\mathbf{r}_1 \in A$ and $\mathbf{r}_2 \in \alpha$, the dominant contribution arises when $\mathbf{r}_4, \mathbf{r}_5 \in \alpha$, $g_m \sim \phi_d$ near the resonance energy $\omega \sim -\varepsilon_d$. The integral over $\mathbf{r}_2$ and $\mathbf{r}_3$ in Eq. (B6) is thus written

$$\sum_{m_d} \int \phi_d^*(\mathbf{r}_2)v(\mathbf{r}_5-\mathbf{r}_2)g_{sc}^{\alpha}(\mathbf{r}_2,\mathbf{r}_3;\omega+\varepsilon_d) \times \Delta(\mathbf{r}_3)\phi_d(\mathbf{r}_3)d\mathbf{r}_2 d\mathbf{r}_3$$

$$= \sum_{m_d}\sum_{LL_1} \frac{4\pi}{2l_1+1} Y_{L_1}^*(\hat{\mathbf{r}}_5)G(L_dL|L_1)G(L_dL|10) \times \int R_{l_d}(r_2)R_{l_d}(r_3)g_l^{\alpha}(r_2,r_3;\omega+\varepsilon_d)r_2^2 r_3^3 \frac{r_<^{l_1}}{r_>^{l_1+1}} dr_2 dr_3, \tag{B9}$$

where $r_>=\max(r_2,r_5)$ and $r_<=\min(r_2,r_5)$. From the orthogonality relation (B4) the above equation is simplified in terms of λ defined by Eq. (12)

$$(B9) = \lambda(\omega+\varepsilon_d,r_5)Y_{10}(\hat{\mathbf{r}}_5). \tag{B10}$$

Next we substitute (B8)–(B10) into (B6), and the most important term of (24) in the order of R_α^{-3} is obtained by use of the above relations

$$(24) \approx \frac{4\pi}{3}\sum_{m_dL}\sum_{m_1m_2} y_{1m_1,1m_2}(\mathbf{R}_\alpha)\langle f_{\mathbf{p}}^- | rY_{1m_2}(\hat{\mathbf{r}})|\phi_c\rangle \times \rho'^{\alpha}(\omega+\varepsilon_d)_l G(L_d10|L)G(L_d1m_1|L)$$

$$= \frac{2l_d+1}{3}\sum_m y_{10,1m}(\mathbf{R}_\alpha)\langle f_{\mathbf{p}}^- | rY_{1m}(\hat{\mathbf{r}})|\phi_c\rangle \times \sum_l \langle l_d0\ 10|l\rangle^2 \rho_d'^{\alpha}(\omega+\varepsilon_d)_l. \tag{B11}$$

Finally we have derived Eqs. (24) and (26).

*Electronic address: hiroko@graduate.chiba-u.jp

[1] W. Bardyszewski and L. Hedin, Phys. Scr. **32**, 439 (1985).
[2] L. Hedin, J. Michiels, and J. Inglesfield, Phys. Rev. B **58**, 15565 (1998).
[3] C. Caroli, D. Lederer-Rozenblatt, B. Roulet, and D. Saint-James, Phys. Rev. B **8**, 4552 (1973).
[4] J. J. Chang and D. C. Langreth, Phys. Rev. B **8**, 4638 (1973).
[5] P. Feibelman and D. E. Eastman, Phys. Rev. B **10**, 4932 (1974).
[6] C.-O. Almbladh, Phys. Scr. **32**, 341 (1985).
[7] T. Fujikawa and H. Arai, J. Electron Spectrosc. Relat. Phenom. **123**, 19 (2002).
[8] T. Fujikawa and H. Arai, Chem. Phys. Lett. **368**, 147 (2003).
[9] A. Kay, E. Arenholz, S. Mun, F. J. Garcia de Abajo, C. S. Fadley, R. Denecke, Z. Hussain, and M. A. Van Hove, Science **281**, 679 (1998).
[10] A. W. Kay, F. J. García de Abajo, S. H. Yang, E. Arenholz, B. S. Mun, N. Mannella, Z. Hussain, M. A. Van Hove, and C. S. Fadley, Phys. Rev. B **63**, 115119 (2001).
[11] F. J. García de Abajo, C. S. Fadley, and M. A. Van Hove, Phys. Rev. Lett. **82**, 4126 (1999).
[12] M. Finazzi, G. Ghiringhelli, O. Tjernberg, L. Duo, A. Tagliaferri, P. Ohresser, and N. B. Brookes, Phys. Rev. B **62**, R16215 (2000).
[13] A. Kikas, E. Nõmmiste, R. Ruus, A. Saar, and I. Martinson, Solid State Commun. **115**, 275 (2000).
[14] D. Nordlunb, M. G. Garnier, N. Witkowski, R. Denecke, A. Nilsson, M. Nagasono, N. Mårtensson, and A. Föhlisch, Phys. Rev. B **63**, 121402(R) (2001).
[15] X. Gao, W. Kuch, F. Offi, S. S. Kang, S. Imada, and J. Kirschner, J. Electron Spectrosc. Relat. Phenom. **123**, 11 (2002).
[16] P. Pervan, M. Milun, and D. P. Woodruff, Phys. Rev. Lett. **81**, 4995 (1998).
[17] R. P. Mikalo, G. Appel, P. Hoffmann, and D. Schmeißer, Synth. Met. **122**, 249 (2001).
[18] Y. F. Hu, G. M. Bancroft, and K. H. Tan, J. Electron Spectrosc. Relat. Phenom. **114–116**, 147 (2001).
[19] V. Carravetta and H. Ågren, Chem. Phys. Lett. **354**, 100 (2002).
[20] H. Arai and T. Fujikawa, Phys. Scr., T **115**, 1091 (2005).
[21] F. Byron and J. C. Joachain, Phys. Rev. A **9**, 2559 (1974).
[22] F. Byron and J. C. Joachain, Phys. Rev. A **15**, 128 (1977).
[23] T. Fujikawa, A. Saito, and L. Hedin, Jpn. J. Appl. Phys., Suppl. **32-2**, 18 (1993).
[24] T. Fujikawa, M. Yimagawa, and T. Miyanaga, J. Phys. Soc. Jpn. **64**, 2047 (1995).
[25] T. Fujikawa, K. Hatada, T. Yikegaki, and L. Hedin, J. Electron Spectrosc. Relat. Phenom. **88**, 649 (1998).

[26] T. Fujikawa, K. Hatada, and L. Hedin, Phys. Rev. B **62**, 5387 (2000).
[27] C. O. Almbladh and L. Hedin, *Handbook on Synchrotron Radiation*, edited by E. E. Koch (North-Holland, Amsterdam 1983), Vol. 1b, p. 607.
[28] T. Fujikawa and H. Arai, Recent Res. Dev. Phys. **4**, 657 (2003).
[29] R. V. Vedrinskii, A. A. Novakovich, V. L. Kraizman, A. G. Bermous, and V. S. Machavariani, Physica B **208–209**, 11 (1995).
[30] L. B. Sorensen, J. O. Cross, M. Newville, B. Ravel, J. J. Rehr, H. Stragier, C. E. Bouldi, and J. C. Woicik, *Resonant Anomalous X-ray Scattering*, edited by G. Materlik *et al.* (North-Holland, Amsterdam, 1994), p. 389.
[31] J. Als-Nielsen and D. McMorrow, *Elements of Modern X-Ray Physics* (Wiley, New York, 2001).
[32] G. A. Rizzi, M. Petukhov, M. Sambi, R. Zanoni, L. Perriello, and G. Granozzi, Surf. Sci. **482–485**, 1474 (2001).
[33] C. S. Fadley, *Synchrotron Radiation Research, Advances in Surface and Interface Science*, edited by R. Bachrach (Plenum, New York, 1992), Vol. 1, p. 421.
[34] T. Fujikawa, J. Phys. Soc. Jpn. **50**, 1321 (1981).
[35] T. Fujikawa, J. Phys. Soc. Jpn. **51**, 251 (1982).
[36] T. Fujikawa, J. Phys. Soc. Jpn. **54**, 2747 (1985).
[37] A. Chasse, J. Phys.: Condens. Matter **11**, 6475 (1999).
[38] P. Rennert, J. Electron Spectrosc. Relat. Phenom. **119**, 1 (2001).
[39] T. Fujikawa, J. Electron Spectrosc. Relat. Phenom. **136**, 85 (2004).
[40] M. L. Goldberger and K. M. Watson, *Collision Theory* (Wiley, New York, 1964).
[41] T. Fujikawa, *Handbook of Thin Films, Materials*, edited by H. S. Nalwa (Academic Press, New York, 2002), Vol. 2, p. 415.
[42] T. Fujikawa and L. Hedin, Phys. Rev. B **40**, 11507 (1989).